Check for updates

View Article Online
View Journal

Journal of Materials Chemistry A

Materials for energy and sustainability

Accepted Manuscript

This article can be cited before page numbers have been issued, to do this please use: F. Baskoro, P. Yang, H. Lin, R. C. Wang, H. Q. Wong, H. Tsai, C. Pao, H. Wu and H. Yen, *J. Mater. Chem. A*, 2025, DOI: 10.1039/D4TA08958H.

Volume 6
Number 12
28 March 2018
Pages 4883-5230

Journal of
Materials Chemistry A
Materials for energy and sustainability
rsc.li/materials-a

ISSN 2050-7488

ROYAL SOCIETY OF CHEMISTRY

COMMUNICATION
Zhenhai Wen *et al.*
An electrochemically neutralized energy-assisted low-cost acid-alkaline electrolyzer for energy-saving electrolysis hydrogen generation

This is an Accepted Manuscript, which has been through the Royal Society of Chemistry peer review process and has been accepted for publication.

Accepted Manuscripts are published online shortly after acceptance, before technical editing, formatting and proof reading. Using this free service, authors can make their results available to the community, in citable form, before we publish the edited article. We will replace this Accepted Manuscript with the edited and formatted Advance Article as soon as it is available.

You can find more information about Accepted Manuscripts in the Information for Authors.

Please note that technical editing may introduce minor changes to the text and/or graphics, which may alter content. The journal's standard Terms & Conditions and the Ethical guidelines still apply. In no event shall the Royal Society of Chemistry be held responsible for any errors or omissions in this Accepted Manuscript or any consequences arising from the use of any information it contains.

View Article Online
DOI: 10.1039/D4TA08958H

ARTICLE

Ultra-low Content Induced Intercalation Anomaly of Graphite Anode Enables Superior Capacity at Sub-zero Temperatures

Febri Baskoro,[a,b] Po-Yu Yang,[c] Hong-Jhen Lin,[a] Robin Chih-Hsing Wang,[d] Hui Qi Wong,[a] Hsinhan Tsai,[e] Chun-Wei Pao,[c] Heng-Liang Wu,*[d,f] and Hung-Ju Yen,*[a]*

Received 00th January 20xx,
Accepted 00th January 20xx

DOI: 10.1039/x0xx00000x

The rapid development of energy storage devices has pushed Li-ion batteries (LIBs) bear down for higher performance, better safety, lower cost, and capable to operate in wide range temperatures. However, most LIBs are used only in favorable environments rather than extreme conditions such as in ocean exploration, tropical areas, high altitude drones, and polar expeditions. When chronically or periodically exposed to these harsh environments, conventional LIBs will fail to operate due to hindered ion conductivity, interfacial issues, and sluggish desolvation of Li-ion. Additionally, graphite has been recognized as the-state-of-the-art LIBs negative electrode due to their mechanical stability, electrical conductivity, cost-efficiency, and abundant availability. However, limited Li^+ storage capacity of 372 mA h g^{-1} via LiC_6 coordination has become a bottleneck and hindered its further application for next-generation LIBs. Here we reported intercalation anomaly under ultra-low graphite content that enables super-lithiation stage in the electrode. The ultrahigh rate capability (2200 mA h g^{-1} at 1C and 1100 mA h g^{-1} at 30C) in graphite anode was achieved by reducing its amount within the electrode and adding more conductive filler in the electrode creating a highly conductive system. When operated at -20 °C, the ultra-low graphite anode keeps 50% capacity (1100 mA h g^{-1}) of room temperature, and ranks the best among LIB anodes toward commercialization. Systematical spectroscopy analysis reveals that additional capacitive behavior and a distinct structural evolution, which leads to Li^+ intercalation anomaly up to LiC_2, within ultra-low graphite content electrode significantly improve graphite electrode capacity beyond 372 mA h g^{-1}. Additionally, when the battery operated at sub-zero temperature, this unique electrode structure with higher conductive environment help to overcome the sluggish desolvation process at interface and slow diffusion in the bulk electrodes. This finding shed a new light in the graphite chemistry and pave the way on the development of anode-less lithium-ion batteries.

Introduction

Li-ion batteries (LIBs) have huge impact to the modern society starting from portable energy storage devices and have been making their way towards electric vehicles application.[1] This wide range applications and increasing energy demand have pushed LIBs to maximize their storage capability and broadening its operation temperature. However, most LIBs researches are primarily focusing on the development of high specific energy materials while the key parameters of energy efficiency regarding their commercialization are often neglected.[2, 3] Thus, next generation of LIBs require not only novel electrode materials which are capable of providing high capacity and robust architectures, but also able to increase energy efficiency by reducing the production cost as well as operate under wide range temperature.[2, 4-6] In this regards, the issue related to decayed performance of LIBs at low-temperatures pops out, which becomes one of the main obstacles to restrict their applications at high altitudes or latitudes, and certain defense and space applications.[7, 8] This issue mainly associated to several factors: low ionic conductivity of electrolyte,[9, 10] limited Li^+ diffusivities,[11, 12] and increased interfacial charge-transfer resistant.[13-15]

In general, a LIB anode experienced multi-stages process during lithiation: First, the Li-ions in solvated form migrate from the bulk electrolyte to the surface of electrode, which resemble from ionic conductivity of the electrolyte. Second, the Li-ions were released from solvated form (desolvation process) at electrode/electrolyte interface. Third, the desolvated Li-ions were further migrate through solid electrolyte interphase (SEI) layer and then into the electrode, which corresponds to the SEI resistance and solid-state diffusion process in the bulk material. Notably, all of these process would be significantly impacted by

---

[a] *Institute of Chemistry, Academia Sinica, Taipei 115, Taiwan. E-mail: hjyen@gate.sinica.edu.tw (H.-J. Yen)*
[b] *Material Science and Engineering Research Group, Faculty of Mechanical and Aerospace Engineering, Institut Teknologi Bandung, Jl. Ganesha 10, Bandung 40132, Indonesia*
[c] *Research Center for Applied Sciences, Academia Sinica, Taipei 115, Taiwan. E-mail: cwpao@gate.sinica.edu.tw (C.-W. Pao)*
[d] *Center for Condensed Matter Sciences, National Taiwan University, Taipei 10617, Taiwan. E-mail: hengliangwu@ntu.edu.tw (H.-L. Wu)*
[e] *Department of Chemical and Biological Engineering, The State University of New York at Buffalo, Buffalo, NY14260, USA*
[f] *Center of Atomic Initiative for New Materials, National Taiwan University, Taipei 10617, Taiwan.*

† Electronic Supplementary Information (ESI) available: Supplementary Notes, Cyclic voltammograms, Galvanostatic profiles, Cycling performance, FESEM images, Raman spectra, *Ex-situ* XPS spectra, Simulated XRD spectra, EIS spectra, Supplementary Tables. See DOI: 10.1039/x0xx00000x

View Article Online
DOI: 10.1039/D4TA08958H

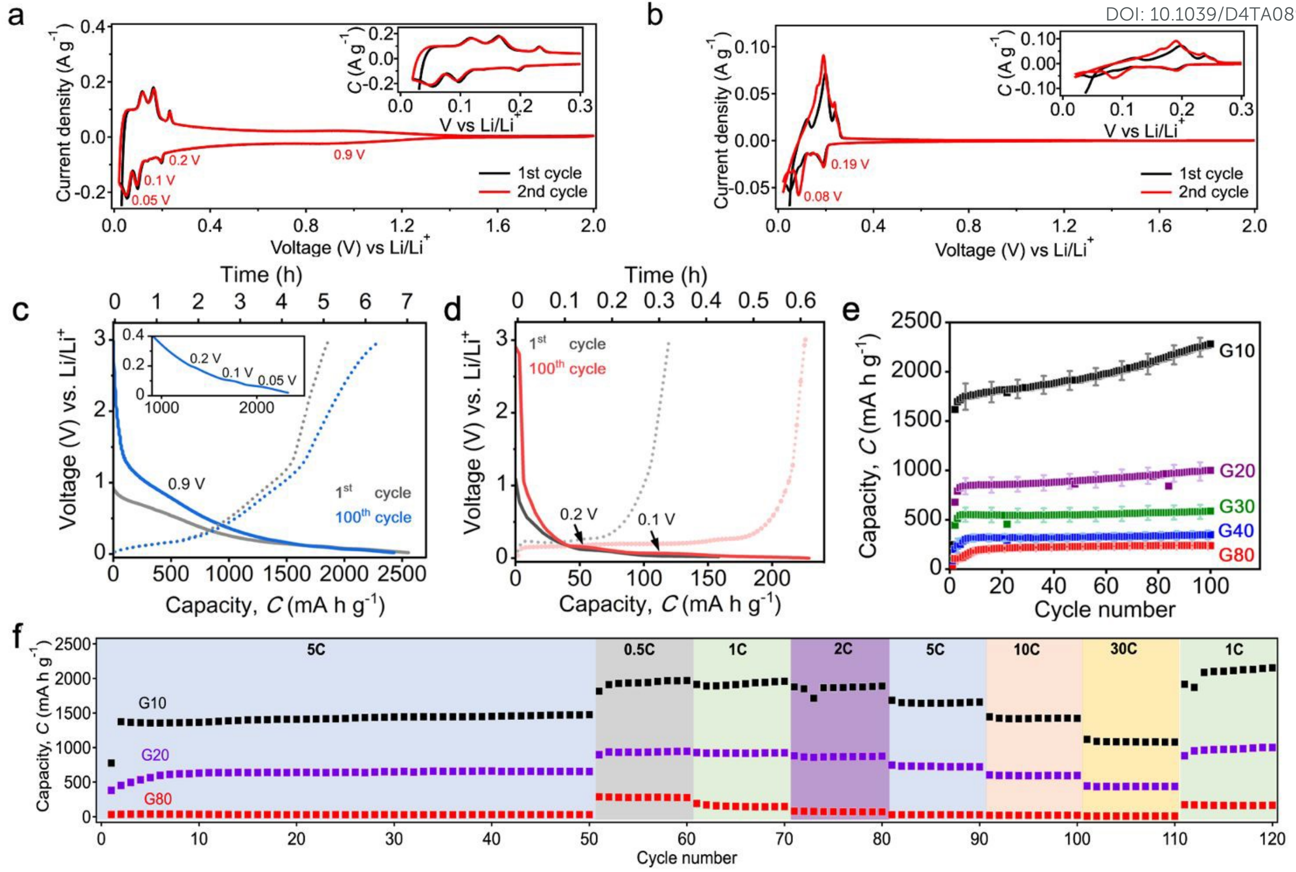

Fig. 1 Electrochemical performance of graphite different content. (a) and (b) are cyclic voltammogram of **G10** and **G80**, respectively. The inset figure is the zoom in on the potential of 0.02 – 0.3 V. (c) and (d) are the selected charge-discharge profile of **G10** and **G80** at 1C (1C: 372 mA h g^{-1}), respectively. (e) The capacity profile of half-cell LIB with different percentage of graphite electrodes. (f) The rate performance of **G10** (black), **G20** (purple), and **G80** (red).

the temperature, especially when the operation temperature dropped to sub-zero. Various approach have been proposed to enhance LIBs performance under low-temperature operation, such as tunning electrolyte composition,[16, 17] developing electrolyte additive,[18-21] and utilizing series of nanostructure materials.[22-25] However, improvement of cycling stability associated with charge-discharge behavior at low temperature are remain very difficult.[19, 26-30]

On the other hand, graphite has been widely used as an anode material due to its excellent mechanical stability, electrical conductivity, abundant availability, and relatively low cost.[1] However, the limited specific capacity of 372 mA h g^{-1}, by only inserting Li^+ to LiC_6 composition between the graphene layers, severely impeded its further application as next generation LIB electrodes.[1, 3, 31] Earlier studies have reported that the specific capacity of graphite can be enhanced beyond LiC_6: the higher specific capacities of graphite with 900 mA h g^{-1}[32] and 1,660 mA h g^{-1}[33] can be achieved by strategies such as heat treatment (pyrolysis at 700 °C) and operated in extreme condition (beyond 100 °C), respectively. Even so, these treatments are considered to be costly thus burden their practical applications. In addition, the mechanism of relatively high specific capacity of graphite is still under debate. Furthermore, several approaches have also been proposed to improve electrochemical performance of graphite under low-temperature operation, such as using mild oxidation,[34, 35] adding metallic particles,[36, 37] chemical doping,[38, 39] and surface coating.[40, 41] Nevertheless, the sluggish desolvation process at interface and slow diffusion in the bulk electrodes was again lead to failure of LIBs at low-temperature.[7, 30, 42, 43]

In the light of high specific capacity and minimal prime cost, here we report Li^+ intercalation anomaly within ultra-low graphite content that dramatically enhance the storage capacity. The reducing graphite weight percentage, while increasing conductive filler, in the electrode is aiming to facilitates capacitive-like behavior and enhance Li^+ diffusivity in the LIBs, which is expected to improve desolvation Li-ions process and interfacial conductivity of graphite anode at low-temperature operation. In brief, various anode electrodes with different graphite content have been fabricated in this study, namely **G10** (graphite 10 wt%), **G20** (graphite 20 wt%), **G30** (graphite 30 wt%), **G40** (graphite 40 wt%), **G80** (graphite 80 wt%); and an electrode without graphite, **SP80**, was also fabricated as a control. Surprisingly, the ultra-low graphite content (**G10** and **G20**) exhibited significant different behavior from that of high graphite content (**G80**). The use of low graphite content anodes, **G10** and **G20**, lead to superior specific capacities of 2200 and 980 mA h g^{-1}, respectively, exceeding the commercial graphite anode (372 mA h g^{-1}) at room temperature. Furthermore, benefiting from the unique features such as high diffusion coefficient and additional pseudocapacitive contribution on the ultra-low graphite content, the **G10** anode exhibited an extremely high low-temperature performance of 1100 mA h g^{-1} (50% capacity retention that that of at room temperature), when it operated at -20 °C. Various electrochemical methods combined with comprehensive characterization techniques as well as simulation studies have been performed to elucidate this distinct anomaly of graphite anodes.

Results and Discussion

In order to probe the behavior of different percentage graphite anodes during insertion/extraction of Li^+, series of electrochemical measurements have been firstly applied in room temperature condition. First, cyclic voltammetry (CV) measurement has been performed to observe the redox potential of different percentage graphite anodes. As shown in Fig. 1a and 1b, four major reduction peaks are monitored on the cathodic scan of **G10** (Fig. 1a), while **G80** (Fig. 1b)exhibited only two major peaks. These multiple reduction peaks on the cathodic scan represented with multi-stages of Li^+ insertion during electrochemical processes.[44, 45] The first peak at ~0.9 V is preferential to the initial stage of lithiation process which is began by Li^+ adsorption on the most outer layers of graphite due to higher conductive environment in the electrode. This distinct Li^+ uptake in the graphitic carbon materials at relatively higher voltage than 0.25 V has also been observed in the previous reports.[32, 46-49] Furthermore, the second peak at 0.2 V can be assigned as the follow up process from Li^+ adsorption process. At this phase, Li^+ starts to insert on the most outer layer of graphite, which could be possibly signed as stage IV intercalation ($30C + Li_{(s)} \rightleftharpoons LiC_{30}$). This process is followed by continuous Li^+ intercalation into more inner layers of graphite, as indicated from the minor peak at 0.15 V, which is an indication of stage III intercalation ($LiC_{36} + Li_{(s)} \rightleftharpoons 2LiC_{18}$). The third and fourth peaks located at 0.1 and 0.05 V are attributed to the further Li^+ intercalation in graphite layers that were presumably linked as deep intercalation stage II ($1/2\ LiC_{18} + Li_{(s)} \rightleftharpoons 3/2\ LiC_6$) and stage I ($6C + Li_{(s)} \rightleftharpoons LiC_6$), respectively.

On the contrary, only two major peaks can only be monitored for **G80** (Fig. 1b) at 0.19 and 0.08 V during cathodic scan, which could be associated to stage IV and stage II intercalation, respectively. The missing reduction peak of ~0.9 and 0.05 V could indicated that a minimum utilization of interlayer graphite under high percentage in the electrode (**G80**). Additionally, the appearance of four major peaks in cathodic scan can also be observed in **G20**, **G30** and **G40** (Fig. S1), indicating an excellent occurrence of Li^+ intercalations into graphitic layers at low graphite content in the electrode. Notably, no redox peaks can be monitored on the **SP80** electrode during CV measurement (Fig. S1d), indicating that no specific redox reaction happen in this electrode during electrochemical process. This further implies that most of electrochemical responses in the CV were contributed from redox reaction within graphite particles.

View Article Online
DOI: 10.1039/D4TA08958H

In agreement with the CV results in Fig. 1a, the galvanostatic charge/discharge profile of **G10** (Fig. 1c) denoted four different plateaus at 0.9, 0.2, 0.1 and 0.05 V, which correlates respectively to their Li^+ intercalation stages during lithiation process. Interestingly, this four plateaus brought significant increase in capacity for **G10** up to 2200 mA h g^{-1} after 100 cycle at 1C. This outstanding specific capacity is nearly six times higher than that of conventional graphite (372 mA h g^{-1}) via LiC_6 formation. Additionally, this four voltage plateaus can also be observed on the **G20**, **G30**, and **G40**, bringing the Li^+ storage capacity beyond 372 mA h g^{-1} (Fig. S2). On the other hand, **G80** only showed two different plateaus at 0.2 and 0.1 V with the specific capacity of 230 mA h g^{-1} at 1C (Fig. 1d). Notably, as applied the same charge-discharge rate of 1C, **G10** exhibited a significantly longer time (~6 hours) to get fully lithiated stage at 0.02 V (Fig. 1c), while **G80** only requires 0.6 hours (Fig 1d). This obvious time difference also suggests that reducing graphite content in the electrode could lighten graphitic layers utilization thus brought a significant impact on achieving extremely high specific capacity. Following the superior performance of **G10**, batteries with **G20**, **G30**, **G40** and **G80** exhibited capacity of ~980 mA h g^{-1}, ~580 mA h g^{-1}, ~340 mA h g^{-1} and ~230 mA h g^{-1}, respectively (Fig. 1e). Furthermore, the extreme rate capability has also been demonstrated for **G10** and **G20** up to 30C (Fig. 1g). Furthermore, **G10** possessed an extremely high rate capability of ~1430 mA h g^{-1} at a relatively high current rate of 30C with excellent stability for up to 2000 cycles (Fig. S3).

To verify the substantial improvement on graphite specific capacity under low percentage, we prepared the **G20** with the increase active material loading into the electrode up to 1.80 mg cm^{-2}. While, we also tried to reduce the loading of **G80** up to 1.19 mg cm^{-2}. Surprisingly, the **G20** electrode with higher loading of 1.80 mg cm^{-2} still hold a high specific capacity of 840 mA h g^{-1} at 1C (Fig. S4a), while **G80** can only deliver capacity of 225 mA h g^{-1}. Moreover, similar trend can also be seen in the rate performance (Fig. S4b) where the **G20** with high material loading could deliver specific capacity of 211 mA h g^{-1} under extremely high current rate of 30 C. Additionally, the specific capacity generated from **SP80** electrode was found to be ~71 mA h g^{-1} under 1C (Fig. S5), indicating that the capacity contributed from the conductive carbon is significantly low compare with the performance of graphite performance under low percentage (**G10** and **G20**). This low specific capacity of **SP80** was consistent with the CV (Fig. S1d), where no specific redox reaction observed during electrochemical process. Therefore, it suggests that graphite intercalation anomaly could possibly occurred under lower active material percentage within the electrode, thus extent and enhance graphite specific capacity beyond 372 mA h g^{-1} (traditional LiC_6 intercalation).[1, 31, 32, 48]

To examine the effect of graphite content on the Li^+ storage mechanism, *ex-situ* XRD measurements of low graphite content

View Article Online
DOI: 10.1039/D4TA08958H

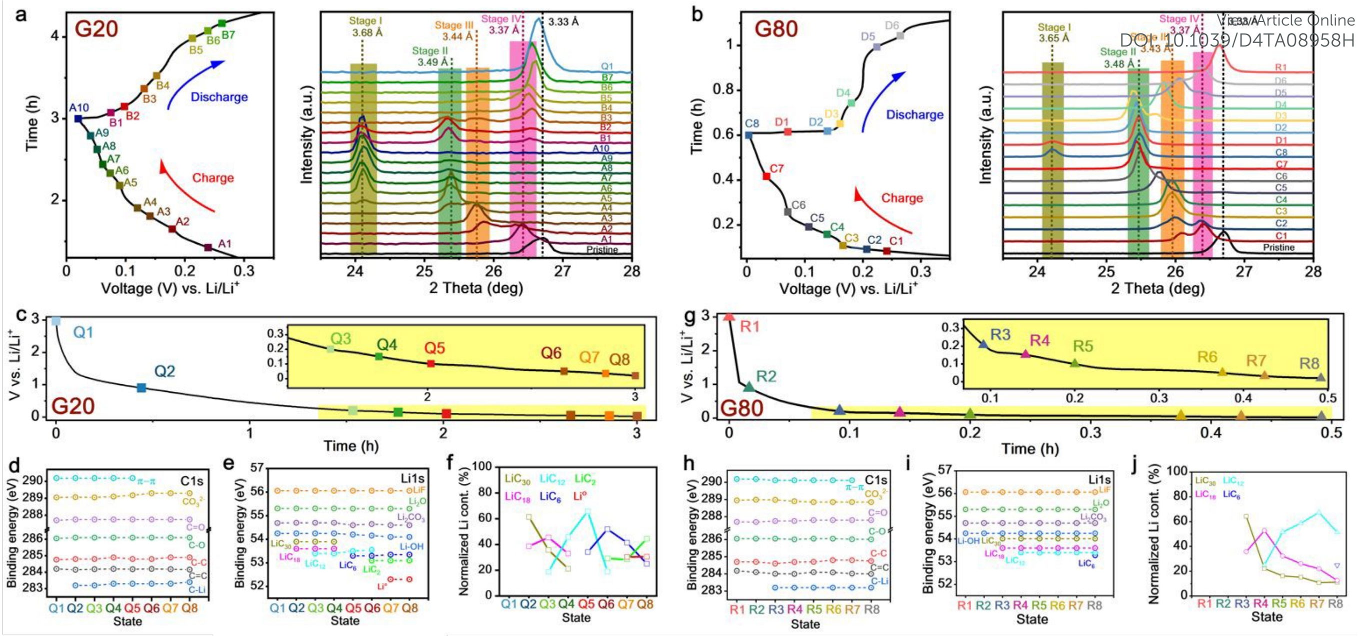

Fig. 2 Systematical analysis of **G20** and **G80** at various stages. (a) Selected stages and *ex-situ* XRD spectra of **G20** at various charge-discharge stages. Charge process: A1 (0.23 V); A2 (0.17 V); A3 (0.14 V); A4 (0.12 V); A5 (0.08 V); A6 (0.07 V); A7 (0.06 V); A8 (0.05 V); A9 (0.04 V); A10 (0.02 V). Discharge process: B1 (0.07 V); B2 (0.09 V); B3 (0.13 V); B4 (0.15 V); B5 (0.21 V); B6 (0.23 V); B7 (0.25 V). (b) Selected stages and *ex-situ* XRD spectra of **G80** at various charge-discharge stages. Charge process: C1 (0.23 V); C2 (0.20 V); C3 (0.17 V); C4 (0.14 V); C5 (0.11 V); C6 (0.07 V); C7 (0.03 V); C8 (0.02 V). Discharge process: D1 (0.07 V); D2 (0.13 V); D3 (0.15 V); D4 (0.18 V); D5 (0.22 V); D6 (0.25 V). (c) Selected states of *ex-situ* XPS analysis on the **G20** during charge process, namely Q1 (3.0 V); Q2 (0.9 V); Q3 (0.2 V); Q4 (0.15 V); Q5 (0.1 V); Q6 (0.05 V); Q7 (0.03 V); Q8 (0.02 V). (d) and (e) C1s and Li1s XPS spectra of **G20** shown at various charge stages. (f) Normalized Li^+ content in **G20** at different charge stages. (g) Selected states on the 2nd charge-discharge process of **G80**, namely R1 (3.0 V); R2 (0.9 V); R3 (0.2 V); R4 (0.15 V); R5 (0.1 V); R6 (0.05 V); R7 (0.03 V); R8 (0.02 V). (h) and (i) C1s and Li1s XPS spectra of **G80** shown at various charge stages. (j) Normalized Li content at different charge state of **G80**.

(**G20**; Fig. 2a) electrode and high graphite content (**G80**; Fig. 2b) electrode were performed to evaluate their structural evolution during Li^+ insertion/extraction. Surprisingly, a distinct structural evolution during Li^+ insertion/extraction can be observed for low graphite content of **G20** than that of **G80** (high graphite content). As shown in Fig. 2a, during the lithiation process from 3.0 to 0.14 V (namely state A1-A3), the diffraction peak of (002) at 26.3° (A1) shifts to a lower value of 25.8° (A3), implying that the graphite interlayer-spacing (*d*-spacing) increases from 3.33 Å (pristine) to 3.37 Å (A1) and then 3.44 Å (A3). This increasing *d*-spacing is a result from early lithiation process associated with the formation of Li^+ intercalation stage IV (LiC_{30}) and stage III (LiC_{18}), respectively, after Li^+ adsorption process on the outer layer of graphite.[44, 50] Furthermore, a twin diffraction peak associated with the *d*-spacing of 3.44 and 3.49 Å, respectively, is obtained at 0.12 V (A4), indicates the transition from Li^+ intercalation stage III to stage II during the further lithiation process (Fig. 2a). In contrast, these intercalation stage III and II of **G80** electrode can only be obtained at deeper lithiation process at 0.07 V (C6) (Fig. 2b). This suggests that low graphite content lighten interlayer utilization than that of higher content. Furthermore, the **G20** electrode with a *d*-spacing of 3.68 Å (24.1°) is obtained at 0.08 V (A5; Fig. 2a), corresponding to the deep Li^+ intercalation of stage I (LiC_6 formation) during the lithiation process.[50] On the contrary, the intercalation stage I can only be slightly observed at 0.02 V in the **G80** electrode (full charge state; C8), along with major contribution of stage II (Fig. 2b). This phenomena further suggests that the low graphite content electrode can be fully lithiated and forms LiC_6 at higher voltage of 0.08 V, while the higher graphite content electrode at the full charged state of 0.02 V is dominated by stage II with minor contribution of stage I, indicating a lighten graphite interlayer utilization.[51, 52] Additionally, the diffraction peak with a *d*-spacing of 3.68 Å on the **G20** gradually become dominant, along with the disappearance of diffraction peak of 25.38° (*d*-spacing of 3.49 Å), as the lithiation process proceed to a deeper potential from A6 (0.07 V) to A10 (0.02 V; full charge stage). This indicates that most of graphite interlayer in the **G20** electrode has been intensively escalate to accommodate large Li^+ intercalation, than that of **G80**. Therefore, these graphite intercalation anomaly based on the *ex-situ* XRD studies of **G20** and **G80** implies that further lithiation process beyond the Li^+ intercalation stage I (LiC_6) possibly taken place during deep charge process of **G20** from A6 (0.07 V) to A10 (0.02 V; full charge stage), thus significantly contribute in boosting the capacity of graphite under low percentage. Moreover, the reaction process is reversible during delithiation process.

View Article Online
DOI: 10.1039/D4TA08958H

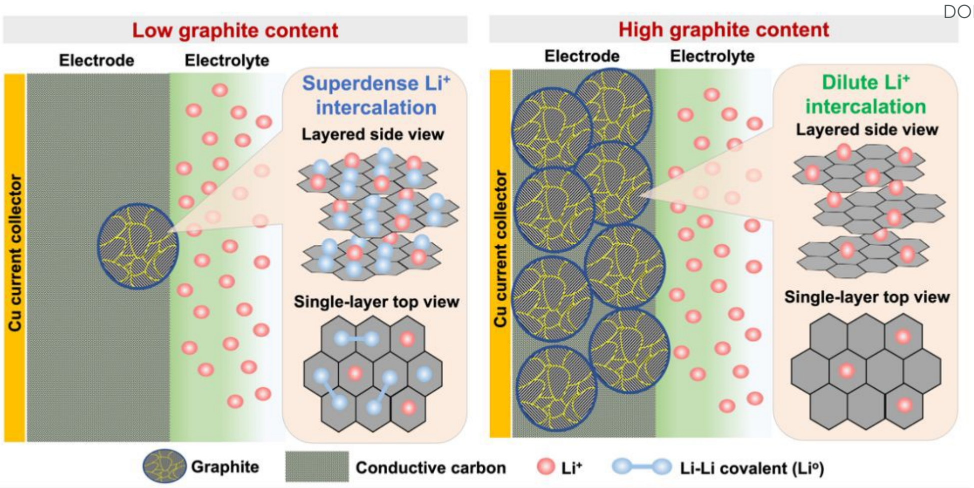

Fig. 3 Schematic illustration for the coexistence of two types of Li site in graphite anodes at low and high content. Graphitic layers are represented by hexagonals. The Li ions and atoms are denoted by red and bule circles, respectively. Covalent bonds between two Li atoms are shown by blue solid lines.

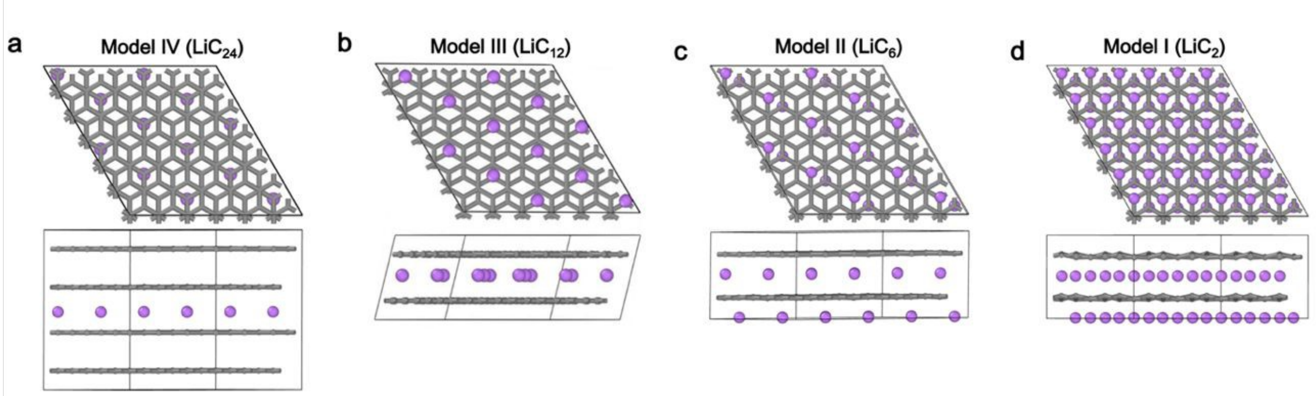

Fig. 4 Li^{+} intercalation models. The top/side views of (a) Model IV (LiC$_{24}$), (b) Model III (LiC$_{12}$), (c) Model II (LiC$_{6}$) and (d) Model I (LiC$_{2}$).

Additionally, field emission scanning electron microscope (FESEM) analysis was performed to probe the morphological changes of graphite particles during electrochemical process. As depicted in Fig. S6b – d, the interlayer of graphite in **G20** was significantly expanded at full-lithiation state (0.02 V). This interlayer expansion could be ascribed to an intensive Li-ion insertion during charge process, which is consistent with the *ex-situ* XRD results, where *d*-spacing of graphite was enlarged from 3.37 (pristine) to 3.68 Å (at full-charge state of 0.02 V) (Fig. 2a). Meanwhile, at the full-discharge state (full de-lithiation at 3.0 V), the well-defined graphite interlayer can be monitored with a minimum expansion (Fig. S6f – h). This phenomena suggests a reversible expansion/relaxation phenomena of graphite interlayers during electrochemical process, and is consistent with the *ex-situ* XRD results. Notably, a similar graphite interlayer expansion can also be monitored at **G20** even after 100 cycles, while no significant changes can be observed for **G80** (Fig. S7). These distinct morphological changes further confirmed an intercalation anomaly of graphite anode under ultra-low content. Furthermore, a distinct graphite morphological evolution was observed in the *ex-situ* Raman spectroscopy of **G10** and **G80** between before and after 100 cycles (Fig. S8). As shown in Fig. S8, typical graphite C-C bonding properties, sp^{3} (D band) and sp^{2} (G band) carbon, can be observed for both **G10** and **G80**. The D band showed no significant changes in **G10** and **G80** after 100 cycles, though, the G band indicated significant peak deformation for **G10**. As depicted in Fig. S8a, the G band peak of **G10**, which originally located 1598 cm^{-1} before cycles, was transformed into two overlapped peaks namely G^{+} (1608 cm^{-1}) and G^{-} (1576 cm^{-1}). However, the G band of **G80** was only slightly shifted from 1590 to 1595 cm^{-1} after 100 cycles (Fig. S8b). The shifting of G band towards the higher wavenumber G^{+} (~1600 cm^{-1}) has been recognized for the intensive interlayer expansion due to the formation of graphite intercalation compound (GIC) from insertion species thus increased the C=C bond length.[53, 54] Meanwhile, the lower wavenumber G^{-} (1576 cm^{-1}) indicated the transformation of sp^{2} carbon bonding configuration or

View Article Online
DOI: 10.1039/D4TA08958H

formation of a shorter sp^2 chain.[55, 56] This *ex-situ* Raman analysis further implied that the graphite under low content in the electrode experienced massive interlayer expansion and structural transformation during cycling process, which might be due to the intensive Li^+ insertion into interlayer of graphite. This observation was again in a good agreement with the *ex-situ* XRD and FESEM analysis.

To gain a further understanding on the chemical bonding during electrochemical process, the *ex-situ* XPS was also performed to evaluate chemical compositions at selected states during 2nd lithiation process, namely states Q1-Q8 for **G20** (Fig. 2c, Fig. S9 and S10) and R1-R8 for **G80** (Fig. 2g, Fig. S11 and S12). The *ex-situ* XPS analysis have been summarized and presented in Fig. 2e – 2f for **G20** and Fig. 2h – 2i for **G80**, respectively. As presented in (Fig. 2d), the C1s spectra at the initial state, 3.0 V (Q1) showed specific binding energy (BE) of C=C, C-C, C-O, C=O, and CO_3^{2-} at 284.21, 284.76, 286.05, 287.7, and 289.05 eV, respectively. A BE associated with the π-π satellite peak can also be observed at 290.19 eV. Furthermore, an additional BE at 283.2 eV associated with C-Li binding started to appear at 0.9 V (Q2) and kept until Q8, indicating the lithiation process (Fig. 2d). Notably, the π-π satellite peak at 290.19 eV disappeared as the Li^+ intercalation reached 0.05 V (Q6) (Fig. 2d), indicating that the π-π interaction between basal planes of graphene were fully utilized to capture Li^+ during intercalation thus results in a weakened interlayer bonding and increased *d*-spacing of graphite, which is in good agreement with the *ex-situ* XRD of **G20** (Fig. 2a). On the contrary, the π-π satellite peak of **G80** is visible from initial state R1 to R7, along with an additional BE at 283.2 eV for C-Li binding started to appear from R3 (Fig. 2h), indicating that the abundant π-π electrons in **G80** are not occupied by Li^+ during charge process. The C1s spectra illustrates that the graphitic interlayers in low graphite content (**G20**) electrode are fully utilized during Li^+ intercalation than that of high graphite content electrode (**G80**). This unique behavior could be possibly responsible for boosting the battery performance.

In good agreement with C1s spectra, the Li1s spectra of **G20** showed the LiC_{30} and LiC_{18} formation with BE of 54.02 and 53.60 eV at 0.9 V (Q2) (Fig. 2e), which has been recognized as Li^+ adsorption on the graphite surface (Fig. 1a).[46, 47] This phenomenon suggested that Li^+ started to intercalate in the outer layer of graphite at 0.9 V (Q2) and results in stage IV and stage III intercalation via formation of LiC_{30} and LiC_{18} during this adsorption process. Furthermore, this process is consistent with *ex-situ* XRD of **G20** ranged from 0.23 to 0.17 V (A1 to A2), in which graphite *d*-spacing increased from 3.33 Å (pristine) to 3.37 and then 3.44 Å (Fig. 2a). As the applied potential is lowered to 0.2 V (Q3), the new BE at 53.40 eV for LiC_{12} appeared along with LiC_{30} and LiC_{18} formation (Fig. 2e), which were no longer observable after 0.05V (Q5). Interestingly, the BE at 53.35 eV for LiC_6 (stage I) begin to form at 0.1 V (Q5), which is in good agreement with *ex-situ* XRD (Fig. 2a), denoting a better utilization of graphite interlayer for **G20** electrode than that of **G80** (Fig. 2b). Furthermore, an additional BE close to the LiC_2 formation appeared at 53.10 eV along with the existence of LiC_{12} and LiC_6 when the applied potential reached 0.05 V (Q6; Fig. 2e). Importantly, when **G20** electrode was fully charged at 0.02 V (Q8), the BE of Li-Li (Li°; 52.3 eV) emerged along with LiC_6 and LiC_2 formation. This co-existing three different Li intercalation species at fully charged state in low graphite content electrode (**G20**) could be responsible for significantly improved Li^+ storage capability. The appearance of Li° BE could be linked to the increased Li metallic character in the state of LiC_2. In the LiC_2 configuration, it was assumed that all the benzene units from the basal plane of graphene were filled with Li ions. Therefore, the continuous insertion of Li^+ in LiC_2 configuration will further push the existing intercalated Li ions getting close one to another, thus increased its metallic character and form Li-Li covalent bonding.[48, 57]

Additionally, the *ex-situ* XPS was also performed for **G10** at different lithiation states, namely states P1-P8, to probe Li^+ intercalation process. As shown in Fig. S13, the **G10** behaves almost identically with the **G20** during lithiation process. The BE at 283.4 eV can be monitored on the C1s spectra since P2 (0.9 V) and kept until P8 (0.02 V), suggesting the formation of C-Li binding during lithiation process (Fig. S13b and S14). Notably, the π-π satellite peak at 290.10 eV for **G10** disappeared when the Li^+ intercalation process reached 0.15 V (P4) (Fig. S13b and S14). This is slightly different than that of **G20**, where the π-π satellite peak disappeared at a lower voltage of 0.05 V (Q6, Fig. 2d) for **G20**, suggesting a better interlayer utilization of **G10** than that of **G20**. Additionally, the L1s spectra of **G10** shows that the Li-Li peak was observed when the lithiation process reached 0.03 V (P7) and 0.02 V (P8; Full-lithiation stage) (Fig. S13c – d), which is consistent with **G20** (Fig. 2e – f). These findings reinforce the notion that under ultra-low content in the anode (**G10** and **G20**), the graphite could behave significantly different than that of high content graphite anode (**G80**).

The *ex-situ* XPS study manifest that further Li intercalation process beyond LiC_6 can be found in the lower graphite percentage (**G10** and **G20**) via formation of LiC_2, indicating an graphite intercalation anomaly under low content electrode. In this intercalation anomaly, a large interlayer expansion of 3.68 Å at the stage of A5 – A10 has opened a channel for further Li intercalation process to form LiC_2. This is in good agreement with the previous study that the superdense Li state (LiC_2) can be formed in the graphitic layers with *d*-spacing of ~3.7 Å,[58, 59] which is close to the *d*-spacing of **G20** at A10 (Fig. 2a). Moreover, another study has also reported that further Li^+ insertion into bilayer of graphitic carbon (Li_xC_6, x>1) will change the atomic state of Li from ionic state to nearly metallic.[60] Additionally, a recent study has also been reported that the LiC_2 domains could co-exist during intercalation process even at a capacity of 524 mA h g^{-1}.[57] On the contrary, Li1s spectra of **G80** in Fig. 2i showed a different Li intercalation behavior than that of **G20** (Fig. 2d and 2e). The formation of LiC_{30} and LiC_{18} in **G80** started from 0.2 V (R3) and remained until fully charged at 0.02 V (R8), while LiC_{12} began to emerge from R4 and dominate in the Li intercalation stage along with the additional LiC_6 formation at R8 (Fig. 2i). This behavior was consistent with the *ex-situ* XRD spectra of **G80** (Fig. 2b). More importantly, the LiC_2 and Li-Li covalent binding cannot be observed in Li1s spectra for **G80** electrode, suggesting a different Li^+ intercalation

View Article Online
DOI: 10.1039/D4TA08958H

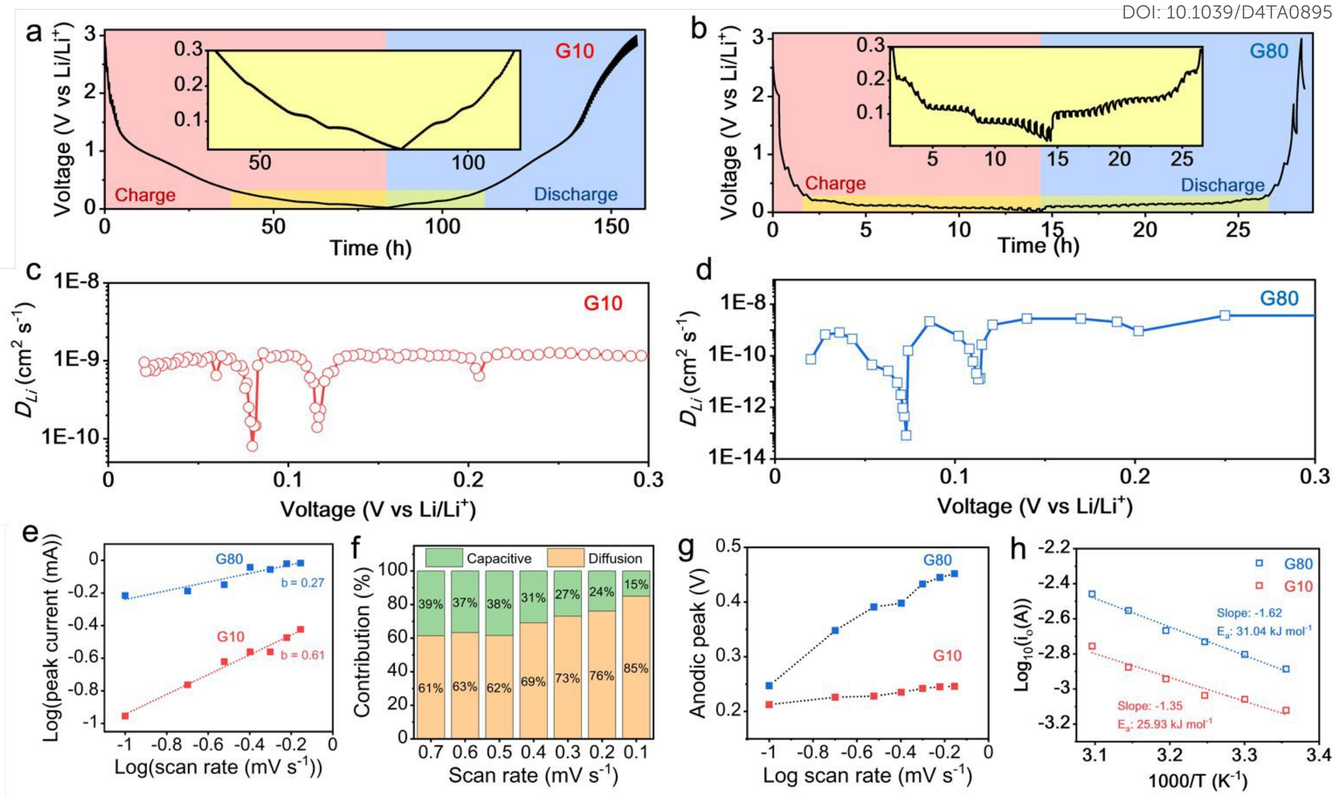

Fig. 5 Kinetical analysis of **G10** and **G80**. (a) and (b) GITT profile of **G10** and **G80**, respectively. (c) and (d) The D_{Li} of **G10** and **G80** during charge process. (e) The *b* value as slope function of Log scan rate (*v*) vs Log peak current (*i*) for **G10** and **G80**. (f) The capacitive and diffusion contribution ratio for **G10** at different scan rates. (g) The anodic peak shift of **G10** and **G80** at various scan rates. (h) Log i_o vs 1000/T plot of **G10** and **G80**.

mechanism to **G20** electrode. The Li1s spectra of **G80** again confirmed that graphite particle behaves significantly different as we lowered the graphite content in the electrode.

Moreover, Fig. 2f depicted the Li-C binding evolution of **G20** at different charging states (Q1-Q8) with appropriate portion contributed in the specific charge, which clearly implies the co-existing three Li intercalation species of LiC_6, LiC_2, and Li-Li covalent bonding formation taken place during lithiation process. However, Li-C binding evolution of **G80** in Fig. 2j reveals that LiC_{12} species dominated Li storage, followed by LiC_6 formation at the full charge state (R8). This distinct intercalation behavior in low and high graphite content electrode manifesting that graphite intercalation anomaly could occurred and boosted the specific capacity of graphite anode. In addition to the contribution of LiC_2 and Li-Li covalent bonding to the battery capacity, another study also reported that the Li storage capacity of carbon materials could be significantly increased up to 990 mA h g^{-1} by formation LiC_2 intercalation.[61] Furthermore, an earlier study by Sato, et. al.[48] reported that Li-Li covalent bonding could be formed and loosely trapped upon two adjacent benzene rings in disordered carbon materials, such as graphite. This Li-Li molecule is able to act as capacity reservoir for increasing capacity up to 1157 mA h g^{-1}. Furthermore, Fig. 3 shows schematic illustration of distinct graphite intercalation behavior under different content in the electrode. As shown in Fig. 3, graphite particles experience Li^+ intercalation anomaly, where most of graphitic layers were utilized to accommodate superdense Li^+ states under low graphite content electrode. In this superdense Li^+ intercalation process, three Li intercalation species of LiC_6, LiC_2, and Li-Li covalent bonding formation co-existed within graphite particles and consequently improved the storage capability. On the contrary, graphite experience dilute Li^+ intercalation state, where LiC_{12} species dominated Li storage, followed by LiC_6 formation.

A series of density functional theory (DFT) calculations were performed to examine the atomistic details of Li^+ intercalation. Four different Li^+ intercalation models corresponding to different intercalation stages based on the theoretical studies by Rüdorff-Hoffman (RH) were constructed and relaxed (see Fig. 4), and the respective simulated XRD spectra, intercalation energies, and capacities were computed and are displayed in Fig. S16 and Table S1, respectively. Comparison of diffraction peaks in Fig. 2a and S16 suggests that the ~24° peak in Fig. 2a (A6 – A10) corresponds to Model I intercalation (LiC_2, Fig. 4d). The simulated diffraction peak from the Model IV intercalation (LiC_{24}, Fig. 4a) is also in agreement with the 25.8° peak (A3) in Fig. 2a. Hence, the DFT calculations confirm the presence of the LiC_2 intercalation. The adsorption energy calculations suggested that the LiC_2 is a metastable state of Li^+ intercalation (see Table S1). It is important to emphasize that the negative adsorption energies observed in this study result solely from the choice of reference configuration. Here, isolated Li atoms in vacuum were used as the reference state. If an alternative reference, such as Li metal, were selected, the adsorption energy would be positive.[57] However, the primary purpose of computing adsorption energies is to gain insight into relative structural stability. Therefore, the absolute sign of the adsorption energy and the specific choice of reference state are not the most critical factors. Moreover, note that the simulated diffraction peaks from Models II and III does not match any peaks displayed in Fig. 2a. In particular, the Model II corresponds to the LiC_6 intercalation, which also yields the lowest adsorption energy (see Table S1). These discrepancies may stem from the limitations of DFT calculations, particularly insufficient energy minimization involving cell dimension optimization due to the high computational cost. In our recent effort to overcome this constraint, we developed a hybrid machine learning (ML) model trained on DFT-calculated energies, particularly in the high-capacity regime, such as LiC_2. This ML model enables large-scale Monte Carlo (MC) simulations of lithium intercalation across a broad range of capacities.[57] The simulation results suggest that lithium intercalation follows a stepwise progression from higher intercalation stages (e.g., stage VI in ref.57) toward stage I, consistent with XRD experiments. Furthermore, our study identifies two new superdense GICs: LiC_4 (524 mA h g^{-1}) and $LiC_{2.6}$ (845 mA h g^{-1}). These phases exhibit interlayer spacings comparable to LiC_6, making them difficult to distinguish from LiC_6 based on XRD data alone. From an energetic standpoint, LiC_4 emerges as the most stable GIC, surpassing even LiC_6, whereas $LiC_{2.6}$ exhibits an intercalation energy similar to that of LiC_6. These findings from extensive MC simulations suggest the feasibility of stable superdense GICs beyond LiC_6. However, it is important to note that the formation of these superdense phases may be kinetically hindered due to sluggish lithium diffusion at higher capacities.

Considering the unique behavior on lighten interlayer utilization to a fully optimized graphitic layer and outstanding Li^+ storage capability at room temperature, the low graphite content presumably allow a rapid Li^+ transport in the electrodes that would be beneficial to overcome the bottleneck of LIB operated at low-temperature. In order to reveal the feasibility of low graphite content as an alternative solution for low-temperature LIB, the galvanostatic intermittent titration technique (GITT) was employed for **G10** and **G80** at 0.1C rate (Supplementary Note 1). Fig. 5a and 5b shows the typical galvanostatic profile of the **G10** and **G80** anodes during GITT measurement, respectively. Interestingly, **G10** has significantly faster Li^+ diffusion coefficient (D_{Li}) of $\sim 10^{-09} – 10^{-10}$ cm^2 s^{-1} than that of **G80** ($\sim 10^{-09} – 10^{-14}$ cm^2 s^{-1}) during lithiation process (Fig. 5c and 5d). As shown in Fig. 5c, the D_{Li} of **G10** dropped up to nearly 10^{-10} cm^2 s^{-1} at potential of ~0.11 and 0.8 V, due to the formation of more compact Li-C species of LiC_{12} and LiC_6, respectively. On the contrary, the D_{Li} of **G80** dramatically slumped up to $\sim 10^{-11}$ and $\sim 10^{-14}$ cm^2 s^{-1} at potential of ~0.11 and 0.8 V (Fig. 5d), indicating a huge barrier for Li^+ mobility in the **G80** during lithiation process. Additionally, a small decrease D_{Li} of **G10** can be monitored at potential ~0.05 V (Fig. 5c), which could be ascribed to formation of superdense Li intercalation (LiC_2). This further suggests that **G10** could provide a significant faster D_{Li} than that of **G80** during phase transitions. This phenomenon could be attributed to the minimum resistances between graphite particles inside of electrode and electrolytes due to higher conductive environment that allowed a rapid electron transfer, therefore accelerate Li^+ transport and improve LIB performance. Furthermore, it was also consistent with previous study that, the increased active material amount within the electrode could impinges the ion transport across the electrode during charge and discharge process.[5] It should be noted that the solid-state Li^+ diffusion acts as a bottleneck for insertion-type materials during the charge storage process, especially at low-temperature.[7, 8, 42] The increasing conductive environment by reducing the graphite content in **G10** enables the fast solid-state diffusion of Li^+ in the bulk electrode, which circumvents the limiting rate of commonly used electrode architecture.

To further probe the ion migration kinetics, a sweep rate CV has been carried out with scan rate ranging from 0.1 to 0.7 mV s^{-1} for both **G10** and **G80** (Fig. S17). According to the power-law relation from sweep rate voltammetry (Supplementary Note 2), the b value of **G10** and **G80** were found 0.61 and 0.27 (Fig. 5e), suggesting the ion migration in **G10** was contributed from diffusion control process and pseudocapacitive behavior simultaneously, while the **G80** was only contributed from diffusion controlled process.[62-64] Further quantitative analysis of diffusion and capacitive contribution (Supplementary Note 2) on the **G10** revealed that the proportion of pseudocapacitive-controlled process at the 0.7 mV s^{-1} was 39 % (Fig. 5f). This contribution gradually decreased up to 15% when the scan rate is lowered to 0.1 mV s^{-1}. This phenomena again confirmed that the Li^+ storage kinetics was controlled by diffusion control process and pseudocapacitive behavior simultaneously. Furthermore, the synergic contribution of both diffusion and pseudocapacitive behavior could further explain the superior performance of low graphite content (see Supplementary Note 2 and 3). Another interesting feature is that the anodic peak of **G10** was not significantly shifted at various scan rates (Fig. 5g), which also identify as combination of diffusion and pseudocapacitive behavior. This such feature has been reported can help overcome the sluggish solid-diffusion process in the electrolyte/electrode interphase,[42] which is considered as one of the most impeding factors for the operation of LIBs at low temperature. Additionally, the electrochemical impedance spectroscopy (EIS) has been employed to evaluate the relationship between exchange current (i_o) and charge transfer resistance at electrode interfaces (R_{ct}) under different temperatures. This correlation help to understand and estimate the activation energy of active materials by using followed Arrhenius equation: $i_0 = RT/nFR_{ct}$, and $i_0 = Aexp(-E_a/RT)$, where A is the temperature-independent coefficient, R represents the gas constant, T is the operating temperature (K),

View Article Online
DOI: 10.1039/D4TA08958H

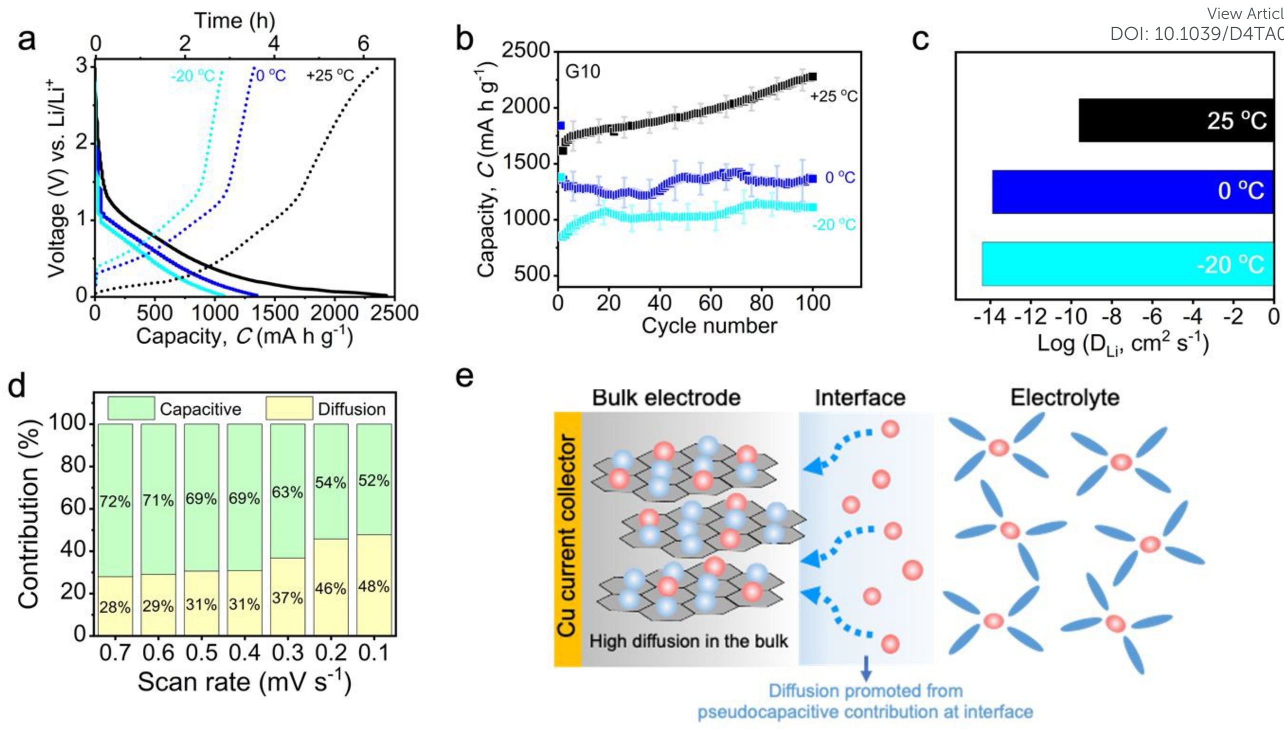

Fig. 6 Low-temperature performance of **G10**. (a) and (b) Galvanostatic and capacity profile at various temperature range, respectively. (c) The D$_{Li}$ at different temperature. (d) The capacitive and diffusion contribution ratio at sub-zero temperature (-20 °C). (e) Schematic illustration of lithiation process of **G10** at low temperature.

n represents the number of electrons being transferred, *F* is the Faraday constant, and E_a represents the apparent activation energy of the active materials in the electrode.[65, 66] Taking these equations, the activation energy is estimated as: $Ea = -Rkln10$, where k is the slope of the fitting line of Arrhenius plots ($Log10i_0$ as a function of 1000/T). Fig. S18 shows the Nyquist plots of **G10** and **G80** electrode at different temperature ranges. As shown in Fig. 5h, the E_a of **G10** and **G80** electrode were estimated to be 25.93 and 31.04 kJ mol^{-1}, respectively. This indicates that reducing graphite content, while increasing the conductive environment in the electrode, could minimized the graphite particle activation energy to store the Li$^+$.

Benefiting from the unique features of high diffusion coefficient and additional pseudocapacitive contribution as well as the reduction of activation energy on low graphite content, the **G10** could possibly overcome the sluggish desolvation process and slow diffusion in LIBs under low-temperature environments. To clarify this point, the electrochemical performance and kinetical study of **G10** at low temperatures were performed and investigated in details, presented in Fig. 6. Fig. 6a showed the galvanostatic charge-discharge profile of **G10** at various temperature after 100 cycles. When the battery was operated 0 °C, **G10** can deliver a capacity of 1250 mA h g^{-1}, corresponding with a high capacity retention of 62.5 % (1250 mA h g^{-1}/2200 mA h g^{-1} = 62.5%). This capacity drop could be resulted from sluggish Li$^+$ diffusion across electrolyte-electrode at low temperature. Surprisingly, when the battery reached at even lower temperature of -20 °C, the specific capacity of **G10** was still kept at 1100 mA h g^{-1} (50% capacity retention), indicating a superior performance at sub-zero temperature. Furthermore, no significant changed can be monitored on the galvanostatic profile of **G10** at low-temperature operation, suggesting a high material stability. In good agreement with the galvanostatic profile, the capacity profile indicates a reduced storage capability from 2200 mA h g^{-1} to 1250 mA h g^{-1} is observed when the operation temperature was lowered from 25 °C to 0 °C (Fig. 6b), respectively, due to limited Li diffusion at low temperature. Notably, the Li storage capacity was only slightly decreased from 1250 mA h g^{-1} to 1100 mA h g^{-1}, when the operation temperature was set at -20 °C. A capacity fluctuation is observed when the battery was operated at 0 °C, and became relatively steady cycling performance at -20 °C. This capacity fluctuation can be associated with the increasing electrolytes viscosity under low-temperature operation.[67] As the operating temperature at 0 °C, the movement of EC molecules is significantly hindered, due to a higher freezing point (~35 °C), than that of DEC at -43 °C, thus creating a binary phase condition in the electrolytes. This condition could possibly disturbing and creating ion flow fluctuation in the electrolyte during charge/discharge process across the cycles, thus resulting a significant capacity fluctuation at 0 °C. However, this binary phase become minimum at -20 °C, as the DEC molecules movement is further minimized, therefore

View Article Online
DOI: 10.1039/D4TA08958H

results in a more steady cycling performance with the decreasing specific capacity up to 1100 mA h g^{-1} (Fig. 6b). In a word, the low graphite content electrode of **G10** demonstrates the highest performance among the reported low-temperature LIBs, in terms of operated temperature, current density and cycling performance (Table S2).

To probe the kinetical phenomena under low-temperature operation, the EIS study was again applied under different temperature. As shown in Fig. S19a and S19b, a significant increase of charge-transfer resistant can be monitored when the operation temperature was lowered from 25 °C to -20 °C, suggesting an increased interfacial charge-transfer at low-temperature. Furthermore, the D_{Li} of **G10** has also showed significant decrease from ~10^{-10} cm^{2} s^{-1} to ~10^{-14} cm^{2} s^{-1} as the operation temperature drops from 25 °C to 0 °C (Fig. 6c), indicating a limited Li diffusion under low temperature (see Supplementary Note 4). Interestingly, the D_{Li} was only slightly shifted to a lower value when the operation temperature reached sub-zero level (-20 °C; Fig. 6c). This indicated that the high conductivity on the bulk electrode is beneficial for maintaining the fast charge-transfer properties, Li^{+} diffusion ability, and battery performance at sub-zero temperature. In addition, sweep rate CV was again employed to dig out the charge mobility under sub-zero temperature. As shown in Fig. S19c, the CV curve of **G10** at sub-zero temperature (-20 °C) was significantly different than that of at 25 °C (Fig. 1a). The well-defined redox peak associated with the Li intercalation at room temperature were hardly observed at -20 °C, showing curves which is similar to pseudocapacitive intercalation behavior (Fig. S19c). Furthermore, the corresponding *b*-value was found to be 0.81, an 0.2 value increased from that of in 25 °C (0.61; Fig. 5f). This suggesting an increased pseudocapacitive contribution during charge-discharge process at -20 °C. The quantitative analysis from total charge stored during sweep rate test at -20 °C further revealed that a high of 72% pseudocapacitive contribution is accumulated at higher scan rate of 0.7 mV s^{-1}, along with significant low of diffusion contribution (28%; Fig. 6d). This pseudocapacitive contribution was then gradually decreased up to 52% at slow scan rate of 0.1 mV s^{-1}, along with increasing diffusion contribution to 48%, indicating the simultaneously contribution of both pseudocapacitive and diffusion during charge-discharge process. As the lithiation process illustrated in Fig. 6e, pseudocapacitive feature of **G10** at low temperature could promote the desolvation process of Li^{+} from electrolyte/electrode at the interphase, while, the fast ions diffusion on **G10** accelerated the migration of Li ions in the bulk electrode. This synergistic contribution of high diffusion coefficient in the bulk electrode and pseudocapacitive contribution turns out to be a perfect combination, which greatly facilitates **G10** with the excellent low temperature performance.

Conclusions

In this work, we observed graphite intercalation anomaly under its low content within the electrode. This intercalation anomaly turns out to be beneficial on boosting the graphite specific capacity and extend its operation range to sub-zero temperature. We believe that this method could be an efficient and effective approach to reduce the production cost of commercial graphite anode in the LIBs. Harnessing the unique feature of lighten interlayer utilization due to fast diffusion, pseudocapacitive contribution, and lower activation energy, low graphite content electrode demonstrated an outstanding specific capacity and ultra-high rate capability of commercial graphite. The use of low graphite content anodes, **G10** and **G20**, leads to superior specific capacities of 2200 and 980 mA h g^{-1}, respectively, exceeding the state of the art graphite anode (372 mA h g^{-1}) at room temperature. Surprisingly, the **G10** anode possess an extremely high capacity of 1100 mA h g^{-1} as operated at sub-zero temperature (-20 °C). This by far is the highest specific capacity recorded at -20 °C. Furthermore, the **G10** anode possess an extremely high capacity of ~1430 mA h g^{-1} at ultra-high current rate of 30C with excellent stability for up to 2000 cycles. The systematical spectroscopy analysis reveals that the origin of this extraordinary performance is due to the synergetic interplay of capacitive contribution and successful formation of superdense Li^{+} intercalation between graphite interlayers. In addition, the perfect combination of high diffusion coefficient in the bulk electrode and pseudocapacitive contribution as well as the reduce graphite activation energy in the electrode greatly enhance the battery performance at low-temperature operation. These results demonstrate the simplest and cheapest attempt to optimize graphite interlayers for Li^{+} storage, pushing the Li-carbon coordination beyond LiC$_{6}$ and unlocking hidden potential of graphite at low-temperature.

Experimental section

Materials

The commercially available natural graphite powder (GN-580L), conductive carbon (Super P®; >99% (metal basis)), polyvinylidene fluoride (PVDF), and 1M lithium hexafluorophosphate (LiPF$_{6}$) in ethylene carbonate (EC) and diethyl carbonate (DEC) (1:1 v/v) were purchased from UBIQ Technology Co., Ltd. *N*-methylpyrrolidone (NMP; >99%) were purchased from Alfa Aesar (Thermo Fisher Scientific). All the materials were used as received without further purification.

Electrode preparation

The graphite electrode with different percentage were prepared by slurry casting method. The recipe graphite electrodes are as follow: **G10** (Graphite 10%; Super P 70%; binder (PVDF) 20%); **G20** (Graphite 20%; Super P 60%; PVDF 20%); **G30** (Graphite 30%; Super P 50%; PVDF 20%); **G40** (Graphite 40%; Super P 40%; PVDF 20%); **G80** (Graphite 80%; Super P 10%; PVDF 10%) and as blank sample **SP80** (Super P 80%; PVDF 20%). First, graphite powder, conductive carbon and binder were mixed together and stirring at 450 rpm for 24 h in room temperature. Second, the slurry then were casted on the Cu current collector and dried on the hot plate at 60 °C for overnight (12 h). Third, the drying process continued in the vacuum oven at 80 °C for another 8h. Finally, the graphite electrodes were cut in circle with

View Article Online
DOI: 10.1039/D4TA08958H

diameter of 12 mm, resulting the electrode area of 1.13 cm^2. The average electrode mass loading for **G10**, **G20**, **G30**, **G40**, **G80**, and **SP80** electrode were maintained 0.76, 0.78, 0.85, 1.00, 2.43, and 0.606 mg cm^{-2}, respectively. These electrodes were then transferred inside of the glovebox for coin cell fabrication.

Electrochemical measurement

All electrochemical performances measurement conducted using CR2032 coin cell which assembled in the glovebox under Argon atmosphere with H_2O and O_2 concentration were kept <1ppm. LIBs half-cell were fabricated in which graphite with different percentage as working electrode and Li metal foil as a counter/reference electrode. Meanwhile, a total of 40 µL of 1M $LiPF_6$ in mixture of Ethylene carbonate (EC):Diethylene carbonate (DEC) (1:1 v/v) was used as an electrolyte. A Celgard 2325 with 18 mm diameter was used as a separator. The cyclic voltammetry were performed using MultiPalmSens4 electrochemical analyzer with open voltage 0.02 – 3.0 V and scan rate of 0.01 mV s^{-1}. The electrochemical impedance spectroscopy (EIS) analysis were conducted before and after battery cycle using CHI electrochemical workstation model 760e with frequency range from 10mHz to 1MHz and amplitude 10mV. The cells were charged and discharge galvanostatically between 0.02 and 3.0 V using AcuTech battery station systems from AcuTech Systems Co.,Ltd. A low temperature reactor Eyela PSL-2500A (Tokyo Rikakikai Co. Ltd) was used to maintain temperature for cycling performance at low temperature condition. Prior the measurement at low temperature, the coincells were prelithiated at 1C rate in room temperature condition. The prelithiated batteries were then kept inside low temperature reactor for 2 h at specified temperature to reach thermal equilibrium prior the measurement. The specific capacity was calculated based on the weight of active materials with respect to different wt% content in the working electrode. Unless it specified, all electrochemical measurements were carried out with at least three replicates to estimates the error and performed in room temperature condition.

Material characterization

The X-ray diffraction spectroscopy (XRD) analysis were performed using D2 phaser XRD from Bruker Co.,Ltd. The X-ray photoelectron spectroscopy (XPS) was performed using an high-resolution XPS PHI-Quantera II, ULVAC-PHI, Inc. The scanning electron microscope (SEM) were performed using Field-Emission Scanning Electron Microscope (FESEM), Ultra Plus - Carl Zeiss. The Raman spectroscopy were performed using a home-built Raman system with 633nm He-Ne laser.

Computational method

In this study, the density functional theory (DFT) calculations were performed using the Vienna ab initio Simulation Package (VASP)[68] with all-electron projected augmented wave (PAW) pseudopotential.[69] The Brillouin zone was sampled by the Monkhorst–Pack method[70] with a grid of 2 × 2 × 4 Γ-centered k-point. For the system with twice the supercell length in the z-direction, the grid was set to 2 × 2 × 2. The electronic occupancies were described by the Gaussian smearing method with a smearing width of 0.05 eV. The Grimme dispersion correction (DFT-D3)[71] was employed to implement the van der Waals interactions, and a kinetic energy cutoff of 500 eV was used for the planewaves. All of pristine and Li-intercalated graphite structures were fully optimized by DFT calculation including the atomic position, simulation cell shapes and Å, which is consistent with the experimental value of 3.33 Å obtained from the XRD analysis. The structures for DFT calculations were constructed based on the Rüdorff-Hoffman (RH) intercalation model.[72-76] Four RH models were constructed, as depicted in Fig. 4. In Models II-IV, the Li atom packing between two adjacent graphene layers follows the conventional LiC_6 type, whereas the Li atom packing was set to LiC_2 in Model I. A series of DFT geometry optimization calculations were performed to investigate the cell size, stable Li adsorption configures as well as the adsorption energies. Table S2† summarizes the adsorption energy E_{ad}, averaged interlayer distance d_{avg} and theoretical capacity of these models. Note the adsorption energy E_{ad} is defined as:

$$E_{ad} = \frac{E_{Li+C} - E_C - nE_{Li}}{n}$$

where E_{Li+C} is the energy of the Li intercalated graphite, E_C is the energy of the pristine graphite, E_{Li} is the energy of one isolated Li atom, and n is the number of adsorbed Li atoms. The Model II model yields the lowest E_{ad} value of -1.867 eV, suggesting it to be the most stable configuration of lithiated graphite. Note that the Model I (packing mode of LiC_2) is still stable after DFT relaxation with a slight increase in E_{ad} relative to other models, suggesting that the Model I is a metastable lithiated state.

Author Contributions

Febri Baskoro: Methodology, Investigation, Formal Analysis, Writing-original draft, Writing-review & editing. **Po-Yu Yang:** Formal Analysis. **Hong-Jhen Lin**, **Robin Chih-Hsing Wang**, **Hui Qi Wong** and **Hsinhan Tsai**: Investigation, Formal Analysis. **Chun-Wei Pao:** Formal Analysis, Conceptualization, Supervision, Writing-review & editing. **Heng-Liang Wu:** Resources, Conceptualization, Supervision, Writing-review & editing. **Hung-Ju Yen:** Conceptualization, Supervision, Methodology, Writing-review & editing. All authors discussed the results and reviewed the manuscript.

Conflicts of interest

There are no conflicts to declare.

Acknowledgements

This work was financially supported by the Ministry of Science and Technology in Taiwan (MOST 108-2113-M-001-023-MY3; MOST 110-2124-M-001-001) and the Innovative Materials and Analysis Technology Exploration in Academia Sinica (AS-iMATE-110-23). F. B. acknowledges the postdoctoral fellowship program supported by Academia Sinica (AS-PD-11201-M04).

Notes and references

1. J. M. Tarascon and M. Armand, *Nature*, 2001, **414**, 359.
2. P. Meister, H. Jia, J. Li, R. Kloepsch, M. Winter and T. Placke, *Chem. Mater.*, 2016, **28**, 7203-7217.
3. S. Goriparti, E. Miele, F. De Angelis, E. Di Fabrizio, R. Proietti Zaccaria and C. Capiglia, *J. Power Sources*, 2014, **257**, 421-443.
4. B. Dunn, H. Kamath and J.-M. Tarascon, *Science*, 2011, **334**, 928.
5. J. Billaud, F. Bouville, T. Magrini, C. Villevieille and A. R. Studart, *Nat. Energy*, 2016, **1**, 16097.
6. N. Nitta, F. Wu, J. T. Lee and G. Yushin, *Mater. Today*, 2015, **18**, 252-264.
7. A. Gupta and A. Manthiram, *Adv. Energy Mater.*, 2020, **10**, 2001972.
8. X. Dong, Y.-G. Wang and Y. Xia, *Acc. Chem. Res.*, 2021, **54**, 3883-3894.
9. E. J. Plichta, M. Hendrickson, R. Thompson, G. Au, W. K. Behl, M. C. Smart, B. V. Ratnakumar and S. Surampudi, *J. Power Sources*, 2001, **94**, 160-162.
10. B. V. Ratnakumar, M. C. Smart and S. Surampudi, *J. Power Sources*, 2001, **97-98**, 137-139.
11. C. K. Huang, J. S. Sakamoto, J. Wolfenstine and S. Surampudi, *J. Electrochem. Soc.*, 2000, **147**, 2893.
12. Z. Syum, T. Billo, A. Sabbah, B. Venugopal, S.-Y. Yu, F.-Y. Fu, H.-L. Wu, L.-C. Chen and K.-H. Chen, *ACS Sustain. Chem. Eng.*, 2021, **9**, 8970-8979.
13. J. Zhang, J. Zhang, T. Liu, H. Wu, S. Tian, L. Zhou, B. Zhang and G. Cui, *Adv. Energy Sustain. Res.*, 2021, **2**, 2100039.
14. S. S. Zhang, K. Xu and T. R. Jow, *Electrochem. Commun.*, 2002, **4**, 928-932.
15. T. Yuan, X. Yu, R. Cai, Y. Zhou and Z. Shao, *J. Power Sources*, 2010, **195**, 4997-5004.
16. M. C. Smart, B. V. Ratnakumar and S. Surampudi, *J. Electrochem. Soc.*, 2002, **149**, A361.
17. M. C. Smart, B. V. Ratnakumar, L. D. Whitcanack, K. B. Chin, S. Surampudi, H. Croft, D. Tice and R. Staniewicz, *J. Power Sources*, 2003, **119-121**, 349-358.
18. A. Tron, S. Jeong, Y. D. Park and J. Mun, *ACS Sustain. Chem. Eng.*, 2019, **7**, 14531-14538.
19. Q. Li, S. Jiao, L. Luo, M. S. Ding, J. Zheng, S. S. Cartmell, C.-M. Wang, K. Xu, J.-G. Zhang and W. Xu, *ACS Appl. Mater. Interfaces*, 2017, **9**, 18826-18835.
20. M. C. Smart, B. V. Ratnakumar, K. B. Chin and L. D. Whitcanack, *J. Electrochem. Soc.*, 2010, **157**, A1361.
21. W. Wang, T. Yang, S. Li, W. Fan, X. Zhao, C. Fan, L. Yu, S. Zhou, X. Zuo, R. Zeng and J. Nan, *Electrochim. Acta*, 2019, **317**, 146-154.
22. Z. Sun, Z. Li, X.-L. Wu, M. Zou, D. Wang, Z. Gu, J. Xu, Y. Fan, S. Gan, D. Han and L. Niu, *ACS Appl. Energy Mater.*, 2019, **2**, 486-492.
23. J. L. Allen, T. R. Jow and J. Wolfenstine, *J. Power Sources*, 2006, **159**, 1340-1345.
24. D. P. Abraham, J. R. Heaton, S. H. Kang, D. W. Dees and A. N. Jansen, *J. Electrochem. Soc.*, 2008, **155**, A41.
25. A. N. Jansen, D. W. Dees, D. P. Abraham, K. Amine and G. L. Henriksen, *J. Power Sources*, 2007, **174**, 373-379.
26. X. Fan, X. Ji, L. Chen, J. Chen, T. Deng, F. Han, J. Yue, N. Piao, R. Wang, X. Zhou, X. Xiao, L. Chen and C. Wang, *Nat. Energy*, 2019, **4**, 882-890.
27. S. Rustomji Cyrus, Y. Yang, K. Kim Tae, J. Mac, J. Kim Young, E. Caldwell, H. Chung and Y. S. Meng, *Science*, 2017, **356**, eaal4263.
28. B. Liao, H. Li, M. Xu, L. Xing, Y. Liao, X. Ren, W. Fan, L. Yu, K. Xu and W. Li, *Adv. Energy Mater.*, 2018, **8**, 1800802.
29. K. Xu, *Chem. Rev.*, 2014, **114**, 11503-11618.
30. G. A. Collins, H. Geaney and K. M. Ryan, *J. Mater. Chem. A*, 2021, **9**, 14172-14213.
31. H.-J. Yen, H. Tsai, M. Zhou, E. F. Holby, S. Choudhury, A. Chen, L. Adamska, S. Tretiak, T. Sanchez, S. Iyer, H. Zhang, L. Zhu, H. Lin, L. Dai, G. Wu and H.-L. Wang, *Adv. Mater.*, 2016, **28**, 10250-10256.
32. J. R. Dahn, T. Zheng, Y. Liu and J. S. Xue, *Science*, 1995, **270**, 590.
33. M. Deschamps and R. Yazami, *J. Power Sources*, 1997, **68**, 236-238.
34. F. Nobili, S. Dsoke, T. Mecozzi and R. Marassi, *Electrochim. Acta*, 2005, **51**, 536-544.
35. M. Mancini, F. Nobili, S. Dsoke, F. D'Amico, R. Tossici, F. Croce and R. Marassi, *J. Power Sources*, 2009, **190**, 141-148.
36. F. Nobili, M. Mancini, S. Dsoke, R. Tossici and R. Marassi, *J. Power Sources*, 2010, **195**, 7090-7097.
37. Y. Yan, L. Ben, Y. Zhan and X. Huang, *Electrochim. Acta*, 2016, **187**, 186-192.
38. F. Lu, J. Liu, J. Xia, Y. Yang and X. Wang, *Ind. Eng. Chem. Res.*, 2020, **59**, 5858-5864.
39. C. Li, Y. Xie, N. Zhang, L. Ai, Y. Liang, K. Tuo, X. Ye, G. Jia and S. Li, *Ionics*, 2019, **25**, 927-937.
40. J. Gao, L. J. Fu, H. P. Zhang, T. Zhang, Y. P. Wu and H. Q. Wu, *Electrochem. Commun.*, 2006, **8**, 1726-1730.
41. A. Friesen, S. Hildebrand, F. Horsthemke, M. Börner, R. Klöpsch, P. Niehoff, F. M. Schappacher and M. Winter, *J. Power Sources*, 2017, **363**, 70-77.
42. X. Dong, Y. Yang, B. Wang, Y. Cao, N. Wang, P. Li, Y. Wang and Y. Xia, *Adv. Sci.*, 2020, **7**, 2000196.
43. G. Zhu, K. Wen, W. Lv, X. Zhou, Y. Liang, F. Yang, Z. Chen, M. Zou, J. Li, Y. Zhang and W. He, *J. Power Sources*, 2015, **300**, 29-40.
44. R. Yazami and P. Touzain, *J. Power Sources*, 1983, **9**, 365-371.
45. D. Aurbach, M. D. Levi, E. Levi, H. Teller, B. Markovsky, G. Salitra, U. Heider and L. Heider, *J. Electrochem. Soc.*, 1998, **145**, 3024-3034.
46. M. Agostini, S. Brutti and J. Hassoun, *ACS Appl. Mater. Interfaces*, 2016, **8**, 10850-10857.
47. L. Shi, Y. Chen, R. He, X. Chen and H. Song, *Phys. Chem. Chem. Phys.*, 2018, **20**, 16437-16443.
48. K. Sato, M. Noguchi, A. Demachi, N. Oki and M. Endo, *Science*, 1994, **264**, 556.
49. J. Hassoun, F. Bonaccorso, M. Agostini, M. Angelucci, M. G. Betti, R. Cingolani, M. Gemmi, C. Mariani, S. Panero, V. Pellegrini and B. Scrosati, *Nano Lett.*, 2014, **14**, 4901-4906.
50. A. Missyul, I. Bolshakov and R. Shpanchenko, *Powder Diff.*, 2017, **32**, S56-S62.
51. Y. Reynier, R. Yazami and B. Fultz, *J. Power Sources*, 2007, **165**, 616-619.
52. N. Li and D. Su, *Carbon Energy*, 2019, **1**, 200-218.
53. C. Sole, N. E. Drewett and L. J. Hardwick, *Farad. Disc.*, 2014, **172**, 223-237.
54. L. J. Hardwick, H. Buqa, M. Holzapfel, W. Scheifele, F. Krumeich and P. Novák, *Electrochim. Acta*, 2007, **52**, 4884-4891.
55. J.-B. Wu, M.-L. Lin, X. Cong, H.-N. Liu and P.-H. Tan, *Chem. Soc. Rev.*, 2018, **47**, 1822-1873.
56. A. C. Ferrari and J. Robertson, *Phys. Rev. B*, 2000, **61**, 14095-14107.
57. P.-Y. Yang, Y.-H. Chiang, C.-W. Pao and C.-C. Chang, *J. Chem. Theo. Comput.*, 2023, **19**, 4533-4545.
58. V. Z. Mordkovich, *Synth. Metals*, 1996, **80**, 243-247.
59. V. A. Nalimova, D. Guérard, M. Lelaurain and O. V. Fateev, *Carbon*, 1995, **33**, 177-181.
60. J.-X. Huang, G. Csányi, J.-B. Zhao, J. Cheng and V. L. Deringer, *J. Mater. Chem. A*, 2019, **7**, 19070-19080.

View Article Online
DOI: 10.1039/D4TA08958H

61. J. Kang, H.-V. Kim, S.-A. Chae and K.-H. Kim, *Small*, 2018, **14**, 1704394.
62. V. Augustyn, J. Come, M. A. Lowe, J. W. Kim, P.-L. Taberna, S. H. Tolbert, H. D. Abruña, P. Simon and B. Dunn, *Nat. Mater.*, 2013, **12**, 518-522.
63. J. Wang, J. Polleux, J. Lim and B. Dunn, *J. Phys. Chem. C*, 2007, **111**, 14925-14931.
64. F. Yu, Z. Liu, R. Zhou, D. Tan, H. Wang and F. Wang, *Mater. Horiz.*, 2018, **5**, 529-535.
65. I. Yamada, Y. Iriyama, T. Abe and Z. Ogumi, *J. Power Sources*, 2007, **172**, 933-937.
66. J. Xu, I.-Y. Jeon, J.-M. Seo, S. Dou, L. Dai and J.-B. Baek, *Adv. Mater.*, 2014, **26**, 7317-7323.
67. A. Belgibayeva, A. Rakhmetova, M. Rakhatkyzy, M. Kairova, I. Mukushev, N. Issatayev, G. Kalimuldina, A. Nurpeissova, Y.-K. Sun and Z. Bakenov, *J. Power Sources*, 2023, **557**, 232550.
68. G. Kresse and J. Furthmüller, *Phys. Rev. B*, 1996, **54**, 11169-11186.
69. G. Kresse and D. Joubert, *Phys. Rev. B*, 1999, **59**, 1758-1775.
70. H. J. Monkhorst and J. D. Pack, *Phys. Rev. B*, 1976, **13**, 5188-5192.
71. S. Grimme, J. Antony, S. Ehrlich and H. Krieg, *J. Chem. Phys.*, 2010, **132**, 154104.
72. W. Rüdorff and U. Hofmann, *Z. Anorg. Allg. Chem.*, 1938, **238**, 1-50.
73. E. P. M. Leiva, E. Perassi and D. Barraco, *J. Electrochem. Soc.*, 2016, **164**, A6154-A6157.
74. M. Otero, A. Sigal, E. M. Perassi, D. Barraco and E. P. M. Leiva, *Electrochim. Acta*, 2017, **245**, 569-574.
75. E. M. Gavilán-Arriazu, J. M. Hümöller, O. A. Pinto, B. A. López de Mishima, E. P. M. Leiva and O. A. Oviedo, *Phys. Chem. Chem. Phys.*, 2020, **22**, 16174-16183.
76. E. M. Gavilán-Arriazu, O. A. Pinto, B. A. López de Mishima, D. E. Barraco, O. A. Oviedo and E. P. M. Leiva, *Electrochim. Acta*, 2020, **331**, 135439.

View Article Online
DOI: 10.1039/D4TA08958H

Data Availability Statement

The data supporting this article have been included as part of the Supplementary Information.